

# Epitaxial-strain-induced polar-to-nonpolar transitions in layered oxides

Xue-Zeng Lu and James M. Rondinelli\*

**Epitaxial strain can induce collective phenomena and new functionalities in complex oxide thin films. Strong coupling between strain and polar lattice modes can stabilize new ferroelectric phases from nonpolar dielectrics or enhance electric polarizations and Curie temperatures<sup>1</sup>. Recently, strain has also been exploited to induce novel metal-insulator transitions<sup>2,3</sup> and magnetic reconstructions<sup>4–7</sup> through its coupling to nonpolar modes, including rotations of  $\text{BO}_6$  transition-metal octahedra<sup>8</sup>. Although large strains are thought to induce ferroelectricity, here we demonstrate a polar-to-nonpolar transition in (001) films of layered  $\text{A}_3\text{B}_2\text{O}_7$  hybrid-improper ferroelectrics with experimentally accessible biaxial strains. We show the origin of the transition originates from the interplay of trilinear-related lattice mode interactions active in the layered oxides, and those interactions are directly strain tunable. Our results call for a careful re-examination of the role of strain-polarization coupling in ferroelectric films with nontrivial anharmonicities and offer a route to search for new functionalities in layered oxides.**

One notable exception to the established strain-induced polarization paradigm occurs in some  $\text{BiFeO}_3$  thin films: a polar-to-nonpolar (P–NP) transition is predicted to occur under exceedingly large compressive strain<sup>9</sup>. This nontrivial phase arises because the stability and crystal structure of bulk  $\text{BiFeO}_3$  (ref. 10) depends on a balance of several interacting ferroelectric (FE), oxygen octahedral rotation (OOR), and oxygen octahedral tilt (OOT) modes. Within this context, an oxide class referred to as hybrid-improper ferroelectrics (HIF)<sup>11</sup> has garnered interest owing to strong anharmonic interactions among polar and nonpolar  $\text{BO}_6$  rotational modes<sup>12,13</sup>. Such multimode interactions are responsible for the appearance of an electric polarization<sup>14</sup> with the layered  $\text{A}_3\text{B}_2\text{O}_7$  Ruddlesden–Popper (RP) structure serving as the scaffolding<sup>11,15,16</sup>: A polar lattice mode ( $Q_{\text{F}_5^-}$ ), OOR ( $Q_{\text{X}_2^+}$ ), and OOT ( $Q_{\text{X}_3^-}$ ) interact through a trilinear term,  $Q_{\text{F}_5^-} Q_{\text{X}_2^+} Q_{\text{X}_3^-}$ , to stabilize the polar ground state structure (that is,  $\text{Cmc}2_1$  symmetry) and induce an electric polarization  $P$ . The first theoretically proposed HIF RP oxides include  $\text{Ca}_3\text{B}_2\text{O}_7$  ( $\text{B} = \text{Ti}$  or  $\text{Mn}$ )<sup>11</sup>, which subsequently have been confirmed through recent experiments on  $(\text{Ca},\text{Sr})_3\text{Ti}_2\text{O}_7$  single crystals<sup>17</sup>,  $\text{Ca}_3\text{Ti}_2\text{O}_7$  and  $\text{Ca}_3\text{Mn}_2\text{O}_7$  polycrystals<sup>18</sup>, and  $\text{Ca}_3(\text{Ti},\text{Mn})_2\text{O}_7$  ceramics<sup>19</sup>. In  $(\text{Ca},\text{Sr})_3\text{Ti}_2\text{O}_7$  single crystals, the existence of a switchable  $P$  under a small electric field was also demonstrated<sup>17</sup>. Because the stability of the HIF state and polarization switching rely on the nontrivial multimode coupling, we predict new strain-induced phases will emerge when multimode interactions significantly contribute to the phase stability.

Here we uncover a P–NP transition in (001)  $\text{Ca}_3\text{Ti}_2\text{O}_7$  (CTO) thin films, predicting a nonpolar (NP)  $\text{Pbcn}$  symmetry phase to be stable at modest biaxial compressive ( $\sim 3.3\%$ ) and

tensile ( $\sim 2.6\%$ ) strains. We show the transition is due to a competition between trilinear-related multimode interactions in the  $\text{Cmc}2_1$  and  $\text{Pbcn}$  phases; it manifests microscopically as a change in the ‘sense’ of the  $\text{TiO}_6$  OOR and antipolar Ca cation displacements between neighbouring two-dimensional perovskite slabs comprising the RP structure. The P–NP transition leads to large changes in the dielectric anisotropy of the film, which could support electric field-tunable dielectric responses near the phase boundary appearing under tensile strain. Finally, we report the P–NP transitions in (001)  $\text{Ca}_3\text{Mn}_2\text{O}_7$  and  $\text{Sr}_3\text{Zr}_2\text{O}_7$  films, indicating the potential generality of the phenomenon in related HIF materials.

We first explore the phase space possible to (001) CTO thin films subjected to biaxial strain using density functional calculations and a sophisticated genetic algorithm for the structure exploration (Methods and Supplementary Table 1). Over the  $-4$  to  $4\%$  strain range, we find the lowest energy phases exhibit either a polar  $\text{Cmc}2_1$  or nonpolar  $\text{Pbcn}$  symmetry (Fig. 1a). The  $\text{Cmc}2_1$  phase is stable from  $-3.3$  to  $2.6\%$  strain, whereas beyond these values a transition into the nonpolar  $\text{Pbcn}$  structure occurs.

In the  $\text{Cmc}2_1$  phase, we find  $P$  increases on applying increasing compressive (negative) to tensile (positive) strain, whereas  $P = 0$  for all strains in  $\text{Pbcn}$  (Fig. 1b). Remarkably, it reaches a value of approximately  $36 \mu\text{C cm}^{-2}$  near the tensile phase boundary (dashed vertical line), which is nearly twice the value of the bulk (strain free) polarization computed for CTO. On traversing the P–NP phase boundaries, the polarization vanishes. This behaviour is in contrast to the conventional intuition that a large epitaxial strain should either further enhance the electric polarization or induce a new ferroelectric phase for the (001) perovskite-structured films. Remarkably, at the tensile phase boundary, we predict the piezoelectric response of monodomain CTO to be  $\sim 90 \text{ pC N}^{-1}$  (calculated in the  $\text{Cmc}2_1$  structure at  $3\%$  strain close to the transition point ( $2.6\%$ ), Supplementary Tables 2–4).

We begin to understand the P–NP transition by examining the crystal structure of the nonpolar phase, comparing it to the polar polymorph through a group theoretical analysis with the  $I4/mmm$  structure as the reference. Figure 1c shows there are three distinct symmetry modes,  $Q$ , present in the  $\text{Pbcn}$  structure: in-plane antiferroelectric (AFE) displacements along  $[\bar{1}10]$ , transforming like irreducible representation (irrep)  $M_5^+$  that alone gives the  $\text{Cmca}$  symmetry; out-of-phase OOR about  $[001]$  ( $X_1^-$ ,  $\text{Ccca}$ ); and out-of-phase OOT about  $[\bar{1}10]$  ( $X_3^-$ ,  $\text{Cmcm}$ ). A comparison of the  $Q$  mode displacements in the  $\text{Cmc}2_1$  structure with those in  $\text{Pbcn}$  reveals that the in-plane FE and in-phase OOR modes in  $\text{Cmc}2_1$  are replaced by in-plane AFE and out-of-phase OOR modes in the  $\text{Pbcn}$  phase, respectively, but with the out-of-phase OOT mode unchanged (Fig. 1c). Similar to how  $P$

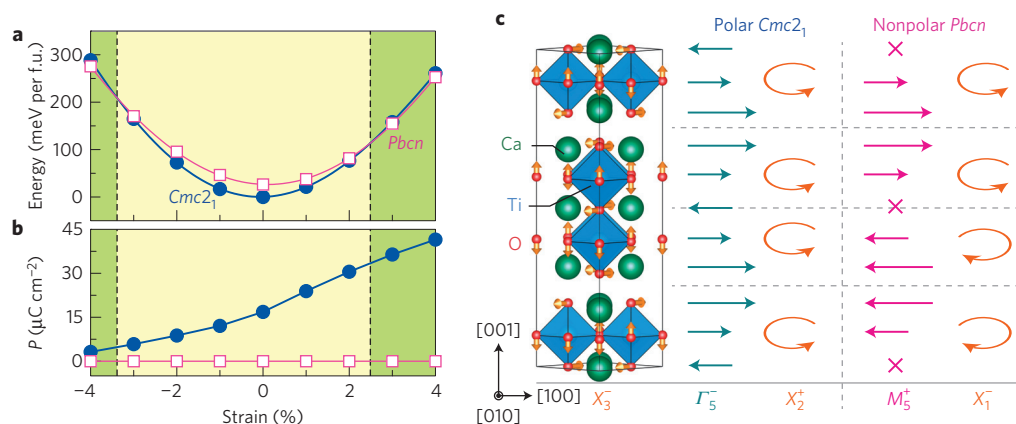


**Figure 1 | Strain dependence of the structure stability and electric polarization for (001)  $\text{Ca}_3\text{Ti}_2\text{O}_7$  films.** **a**, Calculated total energies as a function of biaxial strain, where the energy is given relative to that of the  $\text{Cmc}2_1$  phase at 0% strain. For example at 3% and 4% strains, the nonpolar polymorph is more stable than the polar structure by approximately 3.1 and 8.3 meV per formula unit (f.u.), respectively. The dashed vertical lines indicate the critical strain values for the P–NP transition and separate strain ranges over which the polar (yellow shaded) and nonpolar (green shaded) structures are stable. **b**, Electric polarization versus strain for the polar  $\text{Cmc}2_1$  and nonpolar  $\text{Pbcn}$  phases. **c**, Illustration of the distortion modes in the  $\text{Cmc}2_1$  and  $\text{Pbcn}$  phases with respect to the high-symmetry  $I4/mmm$  reference structure. The structure (left) shows the RP crystal with two-dimensional layers of corner-connected  $\text{TiO}_6$  polyhedra. The arrows on the oxide ions indicate the displacement pattern for the out-of-phase OOT about  $[\bar{1}10]$ , which transforms as irrep  $X_3^-$ . The displacement modes described by  $\Gamma_5^-$  and  $M_5^+$  induce layer polarizations with the direction and magnitude indicated schematically by the teal or pink arrows. Orange arrowed arcs indicate the  $\text{BO}_6$  rotation sense in each perovskite layer. In contrast to the HIF  $\text{Cmc}2_1$  phase, the combination of the  $Q_{X_1^-}$  and  $Q_{X_3^-}$  modes in  $\text{Pbcn}$ , respectively, describing the OOR and OOT, does not lift inversion symmetry. Note that the  $\Gamma_5^-$  mode produces a macroscopic electric polarization, whereas the  $M_5^+$  mode does not induce a macroscopic electric polarization; the cross in  $M_5^+$  indicates there is no layer dipole. The coordinate system is set to a pseudotetragonal system of the perovskite unit cell.

is induced by the OOR and OOT modes in the  $\text{Cmc}2_1$ , the AFE displacements ( $Q_{M_5^+}$ ) in the  $\text{Pbcn}$  structure are also stabilized by anharmonic interactions—that is, the combination of OOR and OOT (Supplementary Fig. 1).

Figure 2a shows that for both phases the OOR decreases when the strain varies from the compressive to tensile, whereas the OOT shows the opposite behaviour. Similar strain induced changes to OOR and OOT were observed in perovskite and perovskite-related films<sup>8,20–23</sup>. Abrupt changes in both OOR and OOT occur at the compressive and tensile P–NP transition boundaries. Unlike the OOT, which are present in both phases, there is a marked change in the sense of the  $\text{TiO}_6$  OOR across the P–NP transition: the in-phase OOR ( $X_2^+$ ) in the  $\text{Cmc}2_1$  phase vanishes and an out-of-phase OOR ( $X_1^-$ ) mode appears in the  $\text{Pbcn}$  structure. The change in the OOR rotation sense induces the AFE mode displacements constrained in the (001) plane, thus affecting the in-plane Ti–O lengths in the  $\text{Pbcn}$  phase (for example, resulting in the two short and two long in-plane Ti–O bonds equal to  $\sim 1.88$  and  $> 2.13$  Å at 3% strain, respectively). The evolutions of the Ti–O lengths (Fig. 2b) and *c*-lattice parameter (Fig. 2c) with strain are similar to those observed in the perovskite films<sup>24,25</sup>, and indicate the  $\text{TiO}_6$  octahedra are not rigid.

The appearance of the AFE  $Q_{M_5^+}$  mode is due to the coupling of  $Q_{X_1^-}$  OOR to the  $Q_{X_3^-}$  OOT through a trilinear term appearing in the free energy. Therefore, we first explore the competition between the  $Q_{X_1^-}$  and  $Q_{X_3^+}$  OORs with respect to biaxial strain to identify the driving force for the P–NP transition. As shown in Fig. 3a, the structure produced solely by the out-of-phase  $Q_{X_1^-}$  OOR mode is always more stable than that produced by the in-phase  $Q_{X_3^+}$  OOR mode. This feature is unable to explain both the stability of the polar  $\text{Cmc}2_1$  phase and the strain-induced P–NP transition.

We thus consider the mode–mode interactions and coupling among the FE (AFE), in-phase OOR (out-of-phase OOR), and OOT degrees of freedom (both OOR and OOT are antiferrodistortive (AFD) distortions) in the  $\text{Cmc}2_1$  ( $\text{Pbcn}$ ) phase using a Landau model. We uniformly write the thermodynamic

free energies ( $E$ ) for the  $\text{Cmc}2_1$  and  $\text{Pbcn}$  phases to fifth order as:

$$E = E_0 + \alpha_i Q_i^2 + \beta_i Q_i^4 + \alpha_j Q_j^2 + \beta_j Q_j^4 + \alpha_k Q_k^2 + \beta_k Q_k^4 + h_0 Q_i Q_j Q_k + h_1 Q_i Q_k Q_j^3 + h_2 Q_i Q_j Q_k^3 + \gamma_{ij} Q_i^2 Q_j^2 + \gamma_{jk} Q_j^2 Q_k^2 + \gamma_{ik} Q_i^2 Q_k^2 \quad (1)$$

where  $E_0$  is the energy of the  $I4/mmm$  structure,  $Q_i$ ,  $Q_j$ , and  $Q_k$  represent the order parameters in units of Å of FE (AFE) [ $i = \Gamma_5^-(M_5^+)$ ], in-phase OOR (out-of-phase OOR) [ $j = X_2^+(X_1^-)$ ] and OOT ( $k = X_3^-$ ) distortions in  $\text{Cmc}2_1$  ( $\text{Pbcn}$ ), respectively, and  $\alpha_{i,j,k}$ ,  $\beta_{i,j,k}$ ,  $h_{0,1,2}$ , and  $\gamma_{i,j,k,ik}$  are the coefficients. (See Supplementary Tables 5–8 for the verification of the model.) Figure 3b shows this minimal model (equation (1)) captures the main features and P–NP transitions appearing in Fig. 1a.

Next, we isolate the contributions from the interactions of the AFD and FE–AFD or AFD and AFE–AFD terms to the total energy gain for the  $\text{Cmc}2_1$  and  $\text{Pbcn}$  phases, respectively, using this model (see Methods). We refer to the interactions that couple the FE or AFE modes with the AFD modes compactly as FE(AFE)–AFD. We find that the biquadratic interaction between the AFD modes contributes more to the stability of the  $\text{Pbcn}$  than the  $\text{Cmc}2_1$  phase in the absence of the FE(AFE)–AFD coupling for all strains explored (Fig. 3c), consistent with the results from Fig. 3a where no coupling terms between  $X_2^+$  ( $X_1^-$ ) and  $X_3^-$  distortions are included. Finally, the FE–AFD interactions over the entire strain region contribute more (filled bars) to the total energy than AFE–AFD couplings (empty bars), as seen in Fig. 3d. Hence, from this energetic comparison we are able to identify that the balance between the FE–AFD and AFE–AFD terms is what controls the P–NP transition.

To understand how strain affects the interacting multimode terms presented in the free energy, we discuss the behaviour within two regions: (I) strain range from  $-4$  to 1% ( $S_1$ ) and (II) strain range

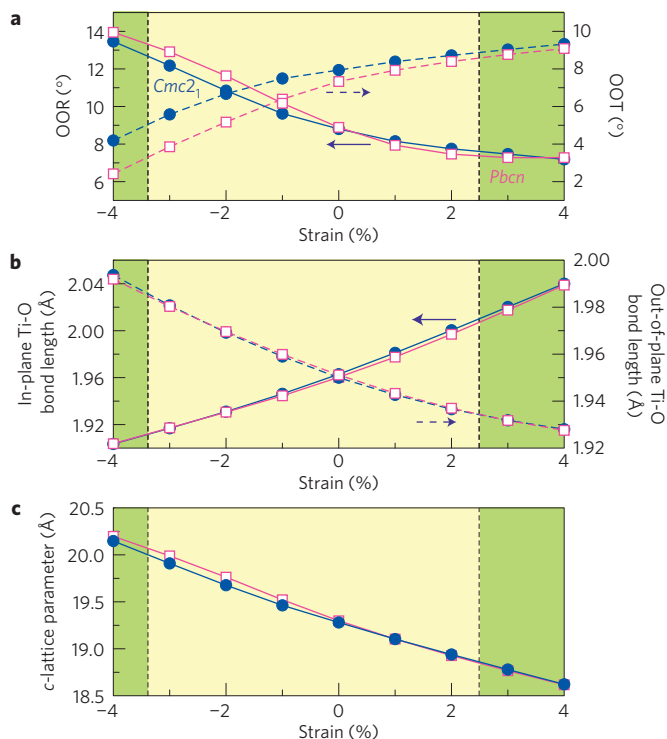


**Figure 2 | Local and crystal structure evolution in  $Ca_3Ti_2O_7$  with biaxial strain.** **a–c**, Calculated OOR and OOT angles (**a**), Ti–O bond lengths (**b**) and c-lattice constant (**c**) as a function of biaxial strain for the  $Cmc2_1$  and  $Pbcn$  phases, respectively. In **b**, the in-plane and out-of-plane Ti–O length values presented are obtained by averaging the equatorial and apical Ti–O bonds in the  $TiO_6$  octahedra, respectively. Note that in **c** the c-lattice parameter at the compressive boundary changes abruptly, which is likely associated with the large differences in the OOT angles between the two phases under those strain values. Thus one avenue to conclusively identify the  $Pbcn$  phase would be to carefully determine the OOR rotation sense and c-lattice constant via X-ray diffraction measurements<sup>24</sup> or microscopy approaches<sup>26</sup>, in addition to the absence of signatures of inversion symmetry, where, for example, optical second harmonic generation should produce no response.

from 1 to 4% ( $S_{II}$ ) (Supplementary Fig. 1). Over  $S_I$ , we find with increasing compressive strain, the AFD distortions are dominant and the contribution from the FE(AFE)–AFD terms to the energy gain in the two phases becomes smaller (see Fig. 3d), indicating the reduced importance of the  $h_0$ ,  $h_1$  and  $h_2$  (odd) terms to the underlying energetic stability of the HIF state. This is because, for the FE(AFE)–AFD interactions, only the odd terms lower the total energy of the polar and nonpolar phases with strain, except at 4% strain. At this 4% strain value, the AFE mode becomes soft and also lowers the total energy (see Methods and Supplementary Fig. 1). Therefore, the reduction in the contribution from the FE–AFD term cannot support the competition of the AFD distortions in  $Cmc2_1$  with the AFD modes preferred in the  $Pbcn$  phase, leading to the transition at  $-3.3\%$ .

In the other strain range ( $S_{II}$ ), the contribution from the FE(AFE)–AFD terms increases with increasing tensile strain, indicating the odd term in the FE(AFE)–AFD coupling becomes more important. We also find that the AFE–AFD contribution increases more rapidly than the FE–AFD contribution. The two contributions from each interaction are nearly comparable at large tensile strain; therefore, when considering the contribution from the AFD distortions, where the FE(AFE)–AFD and AFD terms appearing in equation (1) are relevant (Fig. 3c), the  $Pbcn$  phase

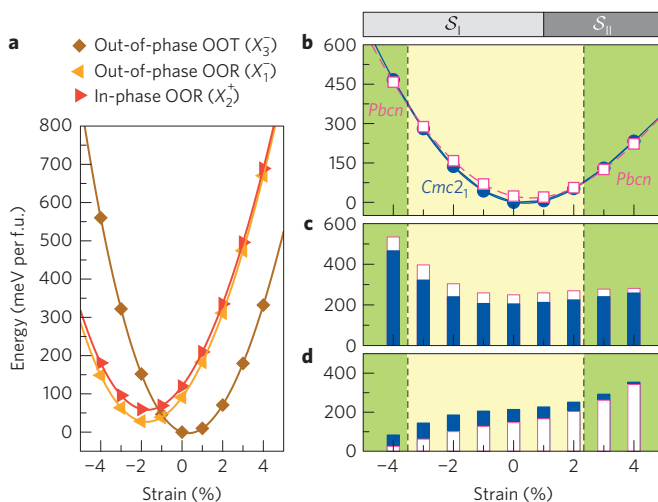


**Figure 3 | Origin of the P–NP transitions with biaxial strain.** **a**, Calculated energies versus strain for the  $Q_{X_3^-}$ ,  $Q_{X_1^-}$  and  $Q_{X_2^+}$  modes. **b**, Stability of the  $Cmc2_1$  and  $Pbcn$  phases with strain based on the Landau phenomenological model (equation (1)). **c,d**, Energy contributions from the AFD (**c**) and FE(AFE)–AFD (**d**) interaction terms to the energy gains with respect to the  $I4/mmm$  structure for each  $Cmc2_1$  and  $Pbcn$  phase, respectively, with strain.

becomes energetically more favourable. Thus, we conclude that the trilinear-related interactions (odd terms) in  $Cmc2_1$  and  $Pbcn$  play both an important role in stabilizing the polar phase for small strain, but also that it is those same terms that have a large strain dependence and induce the P–NP transitions.

We now address the experimental feasibility of realizing the P–NP transitions in CTO. First, the 0 K calculated critical lattice constants for the compressive and tensile phase boundaries are 3.711 Å and 3.937 Å, respectively. The (110)  $YAlO_3$  ( $a = 3.716$  Å) and (110)  $DyScO_3$  ( $a = 3.944$  Å) substrates have suitable lattice constants to stabilize the  $Pbcn$  structure, and nanometre-thick films may be grown before film relaxation (Supplementary Discussion 1). Furthermore, finite-temperature effects will decrease the critical strain value for the phase transition (Supplementary Fig. 2), which may enable the use of additional substrates for epitaxial growth. Experimentally, the presence of a low concentration of oxygen vacancies would weakly increase the critical strain values without any qualitative changes to the P–NP transitions (Supplementary Fig. 3).

Next, we investigate the dielectric response as a function of biaxial strain in the two phases as the permittivity in a proper ferroelectric diverges on approaching a NP–P phase boundary. As shown in Table 1, compressive strain produces a larger average dielectric response ( $\bar{\epsilon}$ ) than tensile strain in both CTO polymorphs. Furthermore, in the  $Cmc2_1$  phase, we find a significant anisotropy ( $\Delta\epsilon_{II}$ ) between  $\epsilon_{11}$  and  $\epsilon_{22}$  in the compressive strain region that gradually disappears at larger tensile strains. Unlike the polar phase, this dielectric anisotropy is also observed for larger tensile strain in the  $Pbcn$  structure. Interestingly, in the two phases,  $\epsilon_{33}$  is much smaller than the in-plane dielectric components, which is unexpected considering that in  $ABO_3$  perovskites  $\Delta\epsilon_{\perp}$  is usually positive<sup>27</sup>. This may be due to the disconnected perovskite blocks along the  $c$ -axis and interlayer interactions that can be tuned with strain-induced changes to the axial ratio. We also find a large difference in the  $\epsilon_{22}$  component along  $b$  between the two phases about the tensile transition boundary, which results from contributions of different low-energy modes (Supplementary Figs 4 and 5). Thus, a tunable dielectric response may be realized, reaching different maxima by varying the frequency of the electric field and temperature<sup>28</sup>,

**Table 1 | Dielectric properties of the polar and nonpolar  $\text{Ca}_3\text{Ti}_2\text{O}_7$  films with biaxial strain.**

Strain	$\epsilon_{ij}$	$\text{Cmc2}_1, \text{Pbcn}$				
		$\epsilon^{\text{ion}}$	$\epsilon^{\text{elec}}$	$\bar{\epsilon}$	$\Delta\epsilon_{\parallel}$	$\Delta\epsilon_{\perp}$
−4	11	60.2, 60.2	5.85, 5.83	59.3, 58.9	−11.2, −12.3	−37.1, −39.8
	22	71.4, 72.5	5.83, 5.83			
	33	29.2, 27.0	5.32, 5.35			
−3	11	65.4, 62.4	5.75, 5.72	60.4, 60.0	−7.52, −13.5	−43.6, −44.6
	22	72.9, 75.9	5.76, 5.72			
	33	26.0, 24.9	5.30, 5.33			
0	11	97.4, 47.5	5.59, 5.48	71.5, 57.6	16.4, −39.0	−69.9, −44.6
	22	81.1, 86.6	5.54, 5.38			
	33	19.5, 22.6	5.39, 5.23			
3	11	39.5, 31.6	5.24, 5.21	34.8, 43.3	6.15, −32.6	−20.6, −29.5
	22	33.7, 64.4	4.98, 5.00			
	33	16.0, 18.6	5.08, 5.05			
4	11	31.5, 26.5	5.13, 5.12	31.0, 37.7	0.027, −27.5	−16.6, −23.2
	22	31.8, 54.4	4.81, 4.80			
	33	14.9, 17.2	5.00, 4.97			

The calculated relaxed-ion ( $\epsilon^{\text{ion}}$ ) and frozen-ion ( $\epsilon^{\text{elec}}$ ) dielectric tensors for  $\text{Cmc2}_1$  (in bold) and  $\text{Pbcn}$  (in italics) phases at select strains in percentages. We define  $\bar{\epsilon} = (\epsilon_{11} + \epsilon_{22} + \epsilon_{33})/3$ ,  $\Delta\epsilon_{\parallel} = \epsilon_{11} - \epsilon_{22}$ , and  $\Delta\epsilon_{\perp} = \epsilon_{33} - (\epsilon_{11} + \epsilon_{22})/2$  as the average dielectric tensor, the  $a$ - $b$  dielectric anisotropy, and  $c$  dielectric anisotropy, respectively, where  $\epsilon_{ij} = \epsilon_{ij}^{\text{ion}} + \epsilon_{ij}^{\text{elec}}$ , ( $ij = 11, 22, 33$ ).

by exploiting the behaviour of  $\epsilon_{22}$  at the tensile P–NP transition (Supplementary Fig. 6).

Last, we find the P–NP transition also appears in (001)  $\text{Ca}_3\text{Mn}_2\text{O}_7$  and  $\text{Sr}_3\text{Zr}_2\text{O}_7$  thin films, where the corresponding bulk (strain free) phases exhibit HIF (Supplementary Fig. 7). Note that bulk  $\text{Ca}_3\text{Mn}_2\text{O}_7$  crystals experimentally exhibit a high-temperature nonpolar polymorph<sup>18</sup>, consistent with our strain-stabilized prediction. In  $\text{Sr}_3\text{Zr}_2\text{O}_7$ , for example, the change in the size of the A- and B-site cations both renormalize the coefficients for the odd-order terms and activate new modes owing to the change in OOT and OOR preferences with composition and strain (Supplementary Fig. 8). The P–NP phase transition seems to be a general feature in epitaxially strained (001) RP thin films exhibiting HIF in bulk; the nonpolar phase should be considered as a competing state when studying the phase diagram, dielectric properties, and  $P$  switching paths of such thin films. Owing to the appearance of the P–NP transition in (001) films of  $\text{Ca}_3\text{Mn}_2\text{O}_7$  and  $\text{Sr}_3\text{Zr}_2\text{O}_7$  and the advances in epitaxial growth of high-quality layered-perovskite oxides<sup>29</sup>, we anticipate that compounds exhibiting multimode anharmonic interactions will serve as a platform to uncover additional hidden functionalities through an improved understanding of strain-induced phenomena.

## Methods

Methods and any associated references are available in the [online version of the paper](#).

Received 6 January 2016; accepted 13 May 2016;  
published online 13 June 2016

## References

- Schlom, D. G. *et al.* Elastic strain engineering of ferroic oxides. *MRS Bull.* **39**, 118–130 (2014).
- Jang, H. W. *et al.* Metallic and insulating oxide interfaces controlled by electronic correlations. *Science* **331**, 886–889 (2011).
- Zhang, J. Y. *et al.* Correlation between metal–insulator transitions and structural distortions in high-electron-density  $\text{SrTiO}_3$  quantum wells. *Phys. Rev. B* **89**, 075140 (2014).
- Lee, J. H. & Rabe, K. M. Epitaxial-strain-induced multiferroicity in  $\text{SrMnO}_3$  from first principles. *Phys. Rev. Lett.* **104**, 207204 (2010).
- Zhai, X. *et al.* Correlating interfacial octahedral rotations with magnetism in  $(\text{LaMnO}_{3+\delta})_N/(\text{SrTiO}_3)_N$  superlattices. *Nature Commun.* **5**, 4283 (2014).
- Moon, E. J. *et al.* Spatial control of functional properties via octahedral modulations in complex oxide superlattices. *Nature Commun.* **5**, 5710 (2014).
- Lu, W. *et al.* Strain engineering of octahedral rotations and physical properties of  $\text{SrRuO}_3$  films. *Sci. Rep.* **5**, 10245 (2015).
- Rondinelli, J. M., May, S. J. & Freeland, J. W. Control of octahedral connectivity in perovskite oxide heterostructures: an emerging route to multifunctional materials discovery. *MRS Bull.* **37**, 261–270 (2012).
- Prosandeev, S., Kornev, I. A. & Bellaiche, L. Phase transitions in epitaxial  $(\bar{1}10)$   $\text{BiFeO}_3$  films from first principles. *Phys. Rev. Lett.* **107**, 117602 (2011).
- Haumont, R. *et al.* Effect of high pressure on multiferroic  $\text{BiFeO}_3$ . *Phys. Rev. B* **79**, 184110 (2009).
- Benedek, N. A. & Fennie, C. J. Hybrid improper ferroelectricity: a mechanism for controllable polarization–magnetization coupling. *Phys. Rev. Lett.* **106**, 107204 (2011).
- Benedek, N. A., Mulder, A. T. & Fennie, C. J. Polar octahedral rotations: a path to new multifunctional materials. *J. Solid State Chem.* **195**, 11–20 (2012).
- Young, J., Stroppa, A., Picozzi, S. & Rondinelli, J. M. Anharmonic lattice interactions in improper ferroelectrics for multiferroic design. *J. Phys. Condens. Matter* **27**, 283202 (2015).
- Bellaiche, L. & Íñiguez, J. Universal collaborative couplings between oxygen–octahedral rotations and antiferroelectric distortions in perovskites. *Phys. Rev. B* **88**, 014104 (2013).
- Harris, A. B. Symmetry analysis for the Ruddlesden–Popper systems  $\text{Ca}_3\text{Mn}_2\text{O}_7$  and  $\text{Ca}_3\text{Ti}_2\text{O}_7$ . *Phys. Rev. B* **84**, 064116 (2011).
- Mulder, A. T., Benedek, N. A., Rondinelli, J. M. & Fennie, C. J. Turning  $\text{ABO}_3$  antiferroelectrics into ferroelectrics: design rules for practical rotation-driven ferroelectricity in double perovskites and  $\text{A}_3\text{B}_2\text{O}_7$  Ruddlesden–Popper compounds. *Adv. Funct. Mater.* **23**, 4810–4820 (2013).
- Oh, Y. S., Luo, X., Huang, F.-T., Wang, Y. & Cheong, S.-W. Experimental demonstration of hybrid improper ferroelectricity and the presence of abundant charged walls in  $(\text{Ca}, \text{Sr})_3\text{Ti}_2\text{O}_7$  crystals. *Nature Mater.* **14**, 407–413 (2015).
- Senn, M. S. *et al.* Negative thermal expansion in hybrid improper ferroelectric ruddlesden–popper perovskites by symmetry trapping. *Phys. Rev. Lett.* **114**, 035701 (2015).
- Liu, X. Q. *et al.* Hybrid improper ferroelectricity in Ruddlesden–Popper  $\text{Ca}_3(\text{Ti}, \text{Mn})_2\text{O}_7$  ceramics. *Appl. Phys. Lett.* **106**, 202903 (2015).
- Zayak, A. T., Huang, X., Neaton, J. B. & Rabe, K. M. Structural, electronic, and magnetic properties of  $\text{SrRuO}_3$  under epitaxial strain. *Phys. Rev. B* **74**, 094104 (2006).
- Johnson-Wilke, R. L. *et al.* Quantification of octahedral rotations in strained  $\text{LaAlO}_3$  films via synchrotron x-ray diffraction. *Phys. Rev. B* **88**, 174101 (2013).
- Rondinelli, J. M. & Coh, S. Large isosymmetric reorientation of oxygen octahedra rotation axes in epitaxially strained perovskites. *Phys. Rev. Lett.* **106**, 235502 (2011).
- Aguado-Puente, P., García-Fernández, P. & Junquera, J. Interplay of couplings between antiferrodistortive, ferroelectric, and strain degrees of freedom in monodomain  $\text{PbTiO}_3/\text{SrTiO}_3$  superlattices. *Phys. Rev. Lett.* **107**, 217601 (2011).
- May, S. J. *et al.* Quantifying octahedral rotations in strained perovskite oxide films. *Phys. Rev. B* **82**, 014110 (2010).



25. Hatt, A. J. & Spaldin, N. A. Structural phases of strained  $\text{LaAlO}_3$  driven by octahedral tilt instabilities. *Phys. Rev. B* **82**, 195402 (2010).
26. Hwang, J., Zhang, J. Y., Son, J. & Stemmer, S. Nanoscale quantification of octahedral tilts in perovskite films. *Appl. Phys. Lett.* **100**, 191909 (2012).
27. Coh, S. *et al.* Si-compatible candidates for high- $\kappa$  dielectrics with the *Pbnm* perovskite structure. *Phys. Rev. B* **82**, 064101 (2010).
28. Lee, C.-H. *et al.* Exploiting dimensionality and defect mitigation to create tunable microwave dielectrics. *Nature* **502**, 532–536 (2013).
29. Lee, J. H. *et al.* Dynamic layer rearrangement during growth of layered oxide films by molecular beam epitaxy. *Nature Mater.* **13**, 879–883 (2014).

## Acknowledgements

We thank L.-F. Huang for helpful discussions. X.-Z.L. and J.M.R. were supported by the National Science Foundation (NSF) through the Pennsylvania State University MRSEC under award number DMR-1420620. DFT calculations were performed on the CARBON cluster at the Center for Nanoscale Materials [Argonne National Laboratory, supported by DOE-BES (DE-AC02-06CH11357)], the Extreme Science and Engineering Discovery

Environment (XSEDE), which is supported by NSF (ACI-1053575), and the DoD Supercomputing Resource Centers supported by the High Performance Computing and Modernization Program of the DOD.

## Author contributions

The study was planned, calculations carried out, and the manuscript prepared by X.-Z.L. and J.M.R. Both authors discussed the results, wrote, and commented on the manuscript.

## Additional information

Supplementary information is available in the [online version of the paper](#). Reprints and permissions information is available online at [www.nature.com/reprints](http://www.nature.com/reprints). Correspondence and requests for materials should be addressed to J.M.R.

## Competing financial interests

The authors declare no competing financial interests.

## Methods

**Ab initio calculations and analyses.** Our total energy calculations are based on density functional theory (DFT) within the generalized gradient approximation (GGA) utilizing the revised Perdew–Burke–Ernzerhof functional for solids (PBEsol)<sup>30</sup> implemented in the Vienna Ab Initio Simulation Package (VASP)<sup>31–33</sup>. We use a 600 eV plane wave cutoff energy for all calculations and the projector augmented wave (PAW) method<sup>34</sup> with the Ca 3s, 3p and 4s electrons, Ti 3p, 3d and 4s electrons, and O 2s and 2p electrons treated as valence states, which give good agreement with the experimental Ca<sub>3</sub>Ti<sub>2</sub>O<sub>7</sub> polar structure (Supplementary Table 9). We also use a  $4 \times 4 \times 1$  *k*-point mesh and Gaussian smearing (0.10 eV width) for the Brillouin-zone integrations. The electric polarization is computed on the basis of linear response theory involving Born effective charges and small ionic displacements with respect to a centrosymmetric reference structure<sup>35</sup>.

To simulate strain in the (001) films, the in-plane lattice vectors are fixed as  $\mathbf{a} = a_s \mathbf{x} + a_s \mathbf{y}$ ,  $\mathbf{b} = -a_s \mathbf{x} + a_s \mathbf{y}$ , where  $a_s$  is the in-plane lattice constant of the substrate imposing the strain (*s*), and  $\mathbf{x}$ ,  $\mathbf{y}$  and  $\mathbf{z}$  are defined within a pseudotetragonal setting. Biaxial strain is then given by  $(a_s - a_0)/a_0$ , where  $a_0$  (3.8376 Å) is the optimized in-plane lattice constant of bulk CTO within the high-symmetry *I4/mmm* reference structure. After imposing the in-plane mechanical constraint, the out-of-plane lattice constant (*c*-lattice parameter) and all internal atomic positions are fully relaxed until the  $\sigma_{zz}$  stress tensor component and maximum force are below  $60 \mu\text{eV} \text{ \AA}^{-3}$  and  $10 \text{ meV} \text{ \AA}^{-1}$ , respectively.

Because *Cmc*2<sub>1</sub> and *Pbcn* phases belong to the *2mm* and *mmm* point groups, respectively, there are only three independent coefficients in the dielectric tensor ( $\epsilon_{11} \neq \epsilon_{22} \neq \epsilon_{33}$ ). To obtain converged results, the planewave cutoff energy is increased to 700 eV. The ionic contributions to the dielectric constant are decomposed into contributions from each phonon mode at 3% strain for each of the *Cmc*2<sub>1</sub> and *Pbcn* phases according to the methods described in ref. 27.

**Genetic algorithm structure search.** We search for low-energy structures that could be stabilized with biaxial strain by utilizing a genetic algorithm (GA) method<sup>36</sup>. At each strain, we perform the GA search several times and set the generation and population size (number of created structures for each generation) to 8 and 16, respectively, in each run. As shown in Supplementary Table 1 we find the centrosymmetric *Pbcn* phase is always a low-energy structure for all strains, competing with the known bulk polar phase.

**Landau model based phase diagram.** In equation (1), we define  $\alpha_j Q_j^2 + \beta_j Q_j^4 + \alpha_k Q_k^2 + \beta_k Q_k^4 + \gamma_{jk} Q_j^2 Q_k^2$  as the AFD term, because these terms contain only OOR and OOT modes. The  $\alpha_i Q_i^2 + \beta_i Q_i^4 + h_{i0} Q_i Q_j Q_k + h_{i1} Q_i Q_j Q_k^3 + h_{i2} Q_i Q_j Q_k^3 + \gamma_{ij} Q_i^2 Q_j^2 + \gamma_{ik} Q_i^2 Q_k^2$  terms in the complete expansion are defined as the FE–AFD or AFE–AFD interaction terms. We also refer to both contributions compactly as FE(AFE)–AFD, because they are associated with the coupling

between FE (or AFE) modes and the AFD modes. We obtain the contribution from the AFD terms to each phase solely with respect to the *I4/mmm* structure at each strain value, whereas the contribution from the FE(AFE)–AFD terms is obtained by subtracting the contribution from the AFD terms from the total energy gain (Fig. 3c,d). Finally the  $\alpha_i Q_i^2 + \beta_i Q_i^4$  terms are also included in the FE(AFE)–AFD term, because they are found to always be positive (reducing the energy gain) in the two phases (except at 4% strain in the nonpolar *Pbcn* phase) owing to the effects of the odd terms (that is,  $h_{i0} Q_i Q_j Q_k + h_{i1} Q_i Q_j Q_k^3 + h_{i2} Q_i Q_j Q_k^3$ ), significantly lowering the total energy to stabilize a larger FE (AFE) distortion.

To obtain the phase diagram appearing in Fig. 3, we minimize the Landau phenomenological expansion obtained using group theory<sup>37</sup> at each strain value by directly carrying out the DFT calculations rather than fitting the coefficients in the expansion. Here the in-plane lattice constant and the normalized *Q* modes considered in equation (1) are constrained, that is, the magnitude of the order parameter is equal to unity and the order parameter direction is also fixed, however, the internal atomic positions are allowed to be optimized according to the directions of the *Q* modes considered (that is, the magnitude of *Q* is relaxed in the optimization) and the *c*-lattice constant is also optimized. This allows us to efficiently and accurately obtain the total energies as described in the Supplementary Information. Note that this method then leads to the  $\Gamma_1^+$  mode, which contains the full symmetry of *I4/mmm*, being omitted in equation (1) and therefore excluded from Fig. 3b. This difference leads to the small variation in the strain–phase stability diagrams appearing in Figs 1a and 3b.

## References

- Perdew, J. P. *et al.* Restoring the density-gradient expansion for exchange in solids and surfaces. *Phys. Rev. Lett.* **100**, 136406 (2008).
- Kresse, G. & Furthmüller, J. Efficient iterative schemes for *ab initio* total-energy calculations using a plane-wave basis set. *Phys. Rev. B* **54**, 11169–11186 (1996).
- Kresse, G. & Furthmüller, J. Efficiency of *ab-initio* total energy calculations for metals and semiconductors using a plane-wave basis set. *Comput. Mater. Sci.* **6**, 15–50 (1996).
- Kresse, G. & Joubert, D. From ultrasoft pseudopotentials to the projector augmented-wave method. *Phys. Rev. B* **59**, 1758–1775 (1999).
- Blöchl, P. E. Projector augmented-wave method. *Phys. Rev. B* **50**, 17953–17979 (1994).
- Meyer, B. & Vanderbilt, D. *Ab initio* study of ferroelectric domain walls in PbTiO<sub>3</sub>. *Phys. Rev. B* **65**, 104111 (2002).
- Lu, X., Gong, X. & Xiang, H. Polarization enhancement in perovskite superlattices by oxygen octahedral tilts. *Comput. Mater. Sci.* **91**, 310–314 (2014).
- Stokes, H. T., Hatch, D. M. & Wells, J. D. Group-theoretical methods for obtaining distortions in crystals: applications to vibrational modes and phase transitions. *Phys. Rev. B* **43**, 11010–11018 (1991).